CHAPTER 18

Laser Tweezers in the Study of Mechanobiology in Live Cells

Elliot L. Botvinick[*] and Yingxiao Wang[†]

[*]Department of Biomedical Engineering, Beckman Laser Institute
University of California, Irvine, California 92612

[†]Department of Bioengineering, Molecular and Integrative Physiology
Neuroscience Program, Beckman Institute for Advanced Science and
Technology, University of Illinois, Urbana-Champaign, Illinois 61801

The study of how cells respond to mechanical stimuli has recently leaped into the forefront of cell science with recent advances in molecular probes facilitating real-time measurements of cell signaling. In this chapter, we will detail the development of a ''real-time'' molecular probe designed to report the current fractional activated state of Src kinase by changing its spectral output in accordance to local Src states. Src kinase is widely understood to be a key player in the transduction of mechanical stimuli transduced through cell adhesions and focal complexes. To study the local and long-range Src response to localized stresses, an experimental protocol was developed whereby ligand-coated microspheres were adhered to the cell surface and pulled laterally by laser tweezers. This chapter contains a practical

METHODS IN CELL BIOLOGY, VOL. 82
Copyright 2007, Elsevier Inc. All rights reserved.

0091-679X/07 $35.00
DOI: 10.1016/S0091-679X(06)82018-2

discussion of system design considerations and force calibration. Image processing, background subtraction, and the construction of an unbiased ratio image are discussed. Methods of analyzing the distribution of activated Src molecules are detailed with examples of cells with varying degrees of mechanostimulation.

I. Introduction

It has become clear that cells can sense their surrounding environment, both chemically and mechanically (Chien *et al.*, 2005). It is, however, not clear how cells perceive the external physical cues and transmit them into intracellular biochemical signals, that is, mechanotransduction. Recent evidence indicates that mechanotransduction is a complex process and many molecules are involved. In particular, integrins, PECAM-1, ion channels, and receptor tyrosine kinases have been implicated to be the mechanosensing elements and trigger intracellular signaling (Chen *et al.*, 1999; Kaufman *et al.*, 2004; Kernan and Zuker, 1995; Wang *et al.*, 1993). Cytoskeletal components, for example actin filaments and microtubules, have been shown to play crucial roles in mediating and transferring subcellular local signals to the whole cell (Ingber, 2003a,b). It appears that different signaling pathways do not function in isolation. Instead, they interact with each other and coordinately regulate cellular functions in response to mechanical stimuli. For example, the activation of VEGF Receptor 2 (Flk-1) by shear stress is dependent on integrins (Wang *et al.*, 2002). Despite these findings, the molecular hierarchy in regulating cellular functions in live cells on mechanical stimulation remains elusive. This chapter describes the design and utilization of Src kinase molecular biosensor to study the real-time spatial response of Src to mechanical stimuli on single cells.

II. Rational

Progress in developing novel fluorescent probes, for example organic dyes and quantum dots, has been enormous in recent years. A large fraction of new probes have been applied not only in basic biological studies but also in molecular imaging, disease diagnostics, and therapeutics. Mechanobiology, as a rapidly developing field, inevitably encompasses the integration and application of these probes. We will briefly describe current research on this aspect not utilizing förster resonance energy transfer (FRET, more commonly referred to as fluorescence resonance energy transfer). In Section III, we will discuss the development of probes using FRET.

A. Fluorescent Probes for Measuring Extracellular Mechanical Stress

Yu-Li Wang has been pioneering the field of measuring the force a cell can exert on the extracellular environment. The protocol he developed has been adopted and used by many other groups. In general, fluorescent beads labeled with either

FITC or Rhodamine are mixed with polyacrylamide. After the polyacrylamide and bead mixture gels, the beads form an irregular grid embedded in the gel. When the cells are cultured on the bead-embedded gel, the force generated by the cells causes the deformation of the gel and displacement of the beads. Since the gel is composed of polyacrylamide, which has a linear stress/strain relationship, the stiffness of the gel can be conveniently controlled by varying the percentage of polyacrylamide in the solution. In a typical experiment, cells are seeded on the gel and as they spread, the positions of the beads change due to stresses the cells exert through their adhesions to the gel. The displaced positions of beads are recorded by a camera. The cells are then trypsinized and rinsed away, and the beads again move as the gel returns to its stress-free state. The bead positions are recorded again. The local displacements of beads before and after the removal of the cells are calculated, which allow the calculation of the stress distribution exerted by the cells on the gel with the help of sophisticated computing algorithm and software (Beningo *et al*., 2001; Pelham and Wang, 1997).

B. Fluorescent Probes for Imaging Intracellular Mechanical Properties

Other fluorescent probes have been employed to study the intracellular mechanics and molecular dynamics. Green fluorescent protein (GFP) and its derivatives, for example yellow fluorescent protein (YFP), have been fused to targeting molecules such that these molecules can lead the fluorescent proteins (FPs) to specific subcellular locations. By monitoring the position changes of these localized fluorescent markers, the intracellular deformation can be mapped out and the *in situ* mechanical properties can be assessed. For example, a YFP-conjugated mitochondria construct has been used to identify the positions of mitochondria. RGF-coated magnetic beads are then allowed to bind to cell membrane receptors, integrins, and adhere on cell surface. Since integrin engagement can induce the coupling between integrins and cytoskeleton, the beads bind tightly to the cell body. The beads are then mechanically perturbed by a three-dimensional magnetic-twisting device (Hu *et al*., 2004). This allows the intracellular mechanical properties to be characterized. This method has revealed an anisotropic mechanical property of cells. In other applications, GFP was fused to vinculin or paxillin. On the local mechanical perturbation of the cell edge using a micropipette, local assembly of focal adhesion complexes was observed, which was shown to be dependent on mDia, but not ROCK pathways (Riveline *et al*., 2001).

III. Methods

A. Designing Custom Probes to Measure Src Kinase Activity

1. Overview of FRET

FRET occurs between two fluorophores if they are in sufficient proximity and if the emission spectrum of the donor fluorophore sufficiently overlaps the excitation spectrum of the acceptor. Any change of the distance and/or relative orientation

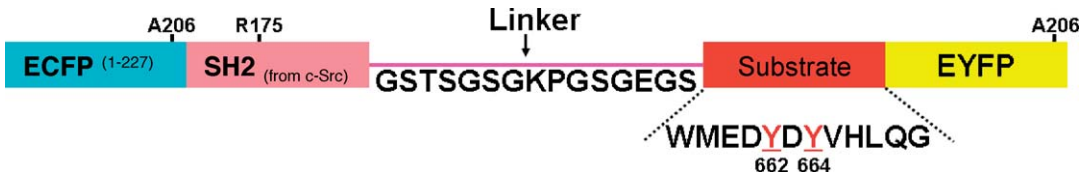

Fig. 1 A schematic cartoon of the Src biosensor composition.

between the two fluorophores may affect the efficiency of FRET and therefore the ratio of acceptor to donor emission (Ting *et al.*, 2001). Previous studies have shown that fusion proteins with interacting peptide partners sandwiched between two different FPs are capable of monitoring various cellular events in live cells with high spatial and temporal resolution (Miyawaki *et al.*, 1997; Tsien, 1998; Zhang *et al.*, 2001).

We have developed a FRET-based biosensor capable of detecting Src kinase activation. As shown in Fig. 1, this genetically encoded biosensor consists of an N-terminal ECFP, an SH2 domain derived from Src kinase, a flexible linker, a substrate peptide specific to Src phosphorylation, and a C-terminal EYFP. When the Src kinase is in its rest state, the ECFP and EYFP are positioned in proximity as a consequence of (1) the tendency of the wild-type ECFP and EYFP to form antiparallel dimmers, (2) the flexible linker, and (3) the juxtaposition of N- and C-terminals of the SH2 domain. Therefore, strong FRET can occur and the excitation of ECYP at 433 nm leads to the emission of EYFP at 527 nm. When Src kinase is activated it phosphorylates the designed substrate peptide, which displays a high affinity to and binds the bottom pocket of the SH2 domain. This action will lead to the displacement of the EYFP from the ECFP and will decrease the FRET efficiency between these two FPs. The excitation of ECFP at 433 nm then results in the emission from ECFP at 476 nm, as shown in Fig. 2. Hence, the emission ratio of ECFP/EYFP with the excitation of ECFP should serve as a good indicator of the status of Src activation.

2. Characterization of the Src Biosensor *In Vitro* and *In Vivo*

We first examined whether the Src biosensor is sensitive and specific to Src kinase. The chimeric Src biosensor proteins were expressed as N-terminal His_6 tag fusions in *E. coli* and purified by nickel chelate chromatography as described previously (Wang *et al.*, 2005). The purified biosensor protein was subjected to an *in vitro* Src kinase assay, in which the fluorescence spectra of the biosensor were monitored by a fluorescence plate reader (TECAN Safire; emission spectra scan at excitation wavelength of 433 nm) to monitor changes in FRET before and after the addition of kinases. The addition of Src kinase and ATP to the Src biosensor caused a 25% loss of FRET by the biosensor, whereas the addition of other kinases, including Yes, FAK, EGFR, Abl, Jak2, or ERK1, caused only very minor FRET change (<2%). Fyn, another member of Src family kinases, caused

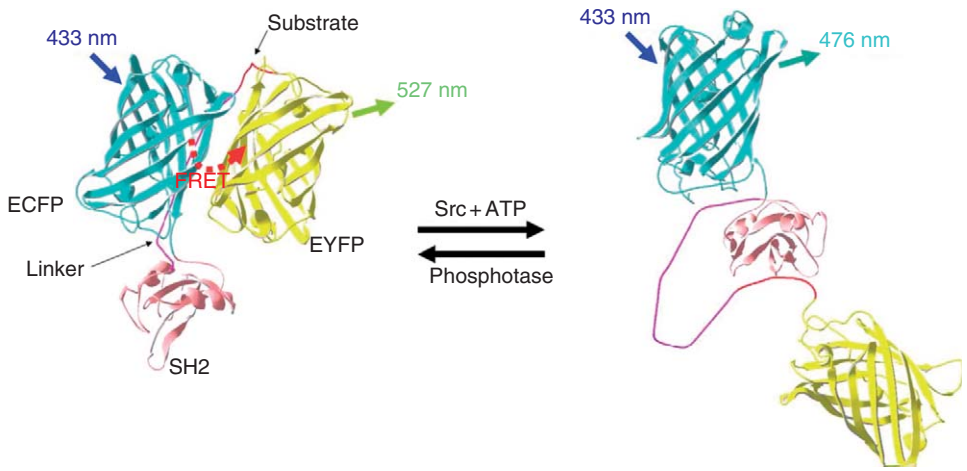

Fig. 2 A schematic cartoon of the activation mechanism of the Src biosensor.

a moderate 10% FRET change of the biosensor. All these results indicate that the Src biosensor is capable of specifically reporting Src activation *in vitro*. We further subcloned the Src biosensor into a PCDNA3.1 vector for mammalian cell expression. The Src biosensor was transfected into HeLa cells, which were subjected to 50-ng/ml EGF to activate Src kinase (Thomas and Brugge, 1997). EGF induced a 25–35% emission ratio change. The EGF-induced FRET response in HeLa cells was reversed by PP1, a selective inhibitor of Src family tyrosine kinases. When HeLa cells were pretreated with PP1 for 1 h, EGF could no longer induce a significant FRET response, suggesting the specificity of the Src biosensor toward Src in mammalian cells.

3. Monomerization of the Src Biosensor

Because the original Src biosensor was irreversible on activation, we reasoned that the tendency of CFP and YFP to form weak antiparallel dimers may be to blame. We modified the original Src biosensor to produce a monomerized Src biosensor by introducing A206K mutations in both ECFP and citrine (EYFP). In HeLa cells, the monomerized biosensor undergoes a dramatic FRET change on Src activation triggered by EGF. The response of the monomerized Src biosensor is also reversible by EGF washout, hence decreasing the Src activity (Fig. 3).

4. Membrane-Targeting Src Biosensor to Plasma Membrane

It has been shown that Src translocation to the plasma membrane is a prerequisite of Src activation (Thomas and Brugge, 1997). To increase the local concentration of the biosensor and position it close to activated Src, we have genetically modified the

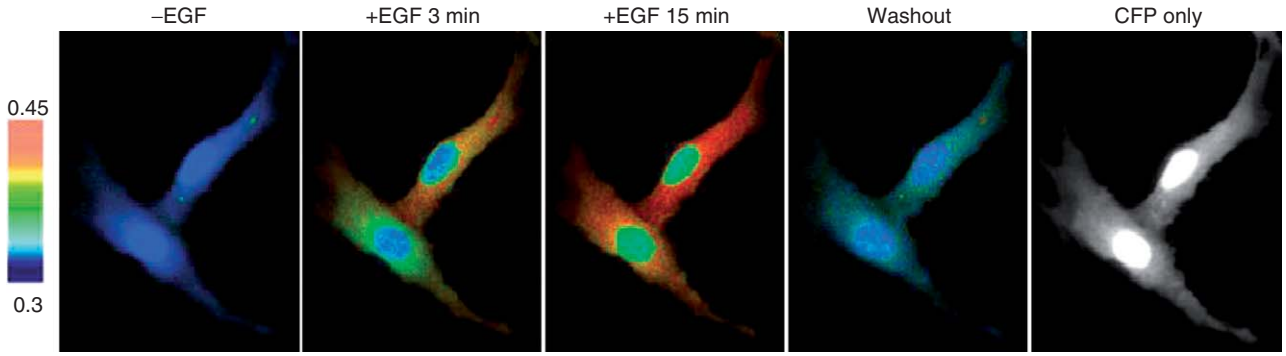

Fig. 3 The monomerized Src biosensor is sensitive to EGF application and reversible on EGF removal. Hela cells were transfected with the monomerized Src biosensor and stimulated with EGF (50 ng/ml) for various time periods as indicated. The cells were subsequently washed with serum-free medium for 15 min (washout). The scale bar on the left represents the CFP/YFP emission ratio, with cold color indicating low Src activity and hot color indicating high levels of Src activation. The representative emission ratio images are shown and the CFP-only image is shown in black and white on the far right.

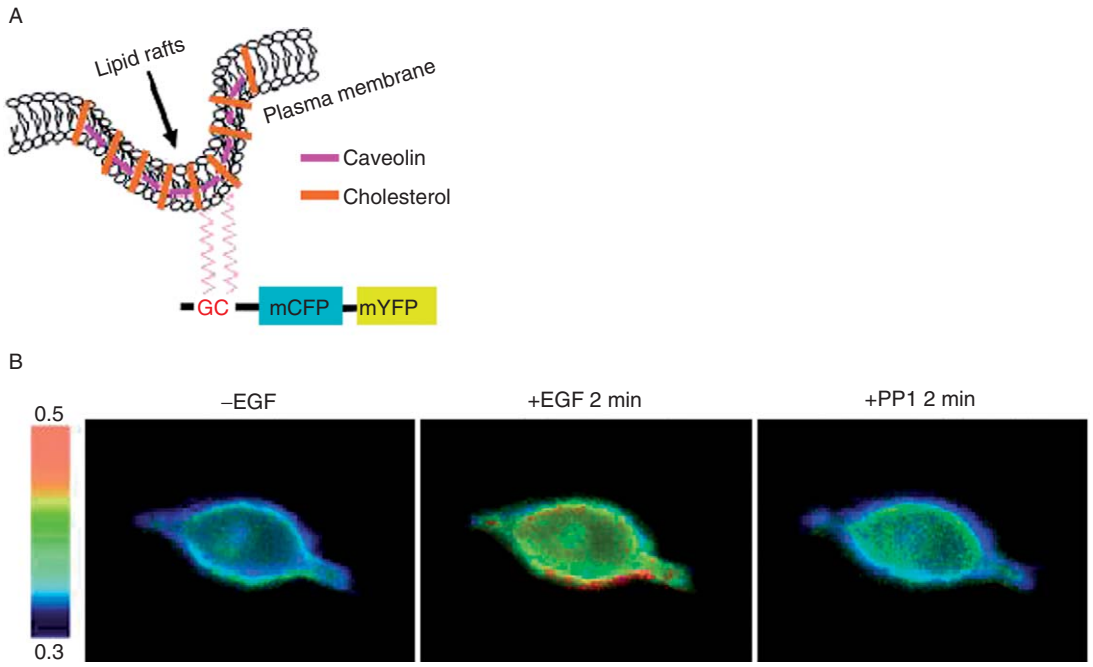

Fig. 4 (A) A schematic cartoon of the modified Src biosensor targeted to the plasma membrane. (B) Hela cells transfected with the membrane-targeted Src biosensor were stimulated with EGF (50 ng/ml) and subsequently incubated with PP1 for the time periods as indicated. The images represent the CFP/YFP emission. The scale bar on the left represents the CFP/YFP emission ratio, with cold color indicating low Src activity and hot color indicating high levels of Src activation.

Src biosensor. A small peptide derived from Lyn kinase was fused to the front of the Src biosensor so that the biosensor can be tethered to the lipid raft domains in the plasma membrane (Fig. 4A). The FRET response of this membrane-targeted Src biosensor can be induced by Src activation on EGF stimulation and inhibited by PP1, a specific inhibitor of Src (Fig. 4). These results indicate that the membrane-targeted Src biosensor is a sensitive and specific indicator of Src activity.

B. Investigation of Mechanotransduction Utilizing FRET Technology and Laser Tweezers

1. Cell Culture Protocol

One important fundamental biological question we want to address is how cells perceive mechanical signals and transmit them into biochemical signals, that is, mechanotransduction. Since we have developed tools capable of visualizing intracellular biochemical activities and perturbing cells mechanically at subcellular

levels, it is natural for us to integrate these two technologies together and investigate the molecular mechanism of mechanotransduction. Since the human umbilical vein endothelial cells (HUVECs) that we are interested in are very difficult to transfect using the lipofectamine method, we first generated a retrovirus version of the Src biosensor (Retromax). The retrovirus carrying the Src biosensor was produced by 293 cells and used to infect HUVECs. The infected cells were serum starved for 24 h before FN-coated beads were seeded onto the cells by the laser tweezers system. Adhesion between FN units and their membrane receptor integrins will induce the adhesion complex to mechanically couple to the cell cytoskeleton. After 20 min of incubation, a calibrated laser tweezers force will be imposed on the bead. The FN-integrin-cytoskeleton coupling then can transmit the force into the cell. FRET responses of the membrane-bound Src biosensor are then monitored and recorded by the fluorescence microscopy system described below.

2. Combining Fluorescence Imaging with Laser Tweezers

Laser tweezers is a method in which the momentum flux of light incident on a particle is transferred, in part, to that particle. When properly constructed, laser tweezers have a local minimum of potential energy within the particle. In this case, the particle can be stably "held" by the focused laser. In our experiments, spherical particles, or microspheres (also referred to as beads in this chapter), are trapped above the focal plane of a high numerical aperture (NA) microscope objective lens within an inverted microscope. To gain a better understanding of the principles of optical tweezers, we highly recommend either Ashkin's paper (Ashkin, 1992) or the Chapter 6 by Nieminen *et al.*, this volume.

The method described below combines both laser trapping of microspheres and fluorescence imaging of a FRET biosensor. Emphasis will be placed on combining the trapping laser and fluorescence excitation light into the microscope, calibrating and applying forces to a microscope attached to the cell surface, and acquiring and calculating the FRET image.

The four manufacturers of research-quality inverted microscopes, have recently modified their platforms or developed add-ons to ease the combination of laser tweezers and nonlaser-based fluorescence excitation. Our laboratory has modified three Carl Zeiss microscopes Nikon (Nikon, Melville, NY), Olympus (Olympus, America, Center Valley, PA), Leica (Leica Microsystems GmbH, Wetzlar, Germany), and Zeiss (Carl Zeiss MicroImaging, Inc., Thornwood, NY), to combined arc lamp excitation and laser tweezers, each in their own way. The three systems have been named RoboLase I, RoboLase II, and RoboLase III. The microscopes implement infinity-corrected optics thereby creating an "infinity space" between the back of the objective and the tube lens of the microscope. Light originating from in-focus objects exits the back of the objective lens and travels through the infinity space as a set of diverging plane waves. The plane waves are refocused by the tube lens to form an image at the intermediate image plane where imaging devices or light detectors are typically mounted. The way to think about combining the light paths is to first

consider the fluorescence filter cube placed in the infinity space. The primary function of the filter cube is to house a dichroic filter. The dichroic filter is responsible for directing incoming fluorescence excitation wavelengths and for transmitting outgoing fluorescence emission to/from the objective lens. The dichroic filter reflects light exiting the epi-illumination lens system housed at the back of the microscope stand up through the back aperture of the objective lens. In a correctly aligned Köhler-illuminated epifluorescence system, the arc lamp is imaged (after reflection from the dichroic filter) onto the back focal plane of the objective lens, thus illuminating the specimen plane with a reasonably uniform distribution of plane waves. Spherical waves of fluorescence emission are subsequently collected by the objective lens to exit its back aperture as a diverging set of plane waves incident on the dichroic filter. The filter cube may also hold an exciter filter with a designed passband of excitation wavelengths and an emitter with a designed passband of emission wavelengths. The emitter has sharp cutoff to remove any excitation light which may be scattered or partially back-reflected within the system.

To add laser tweezers to the microscope, the laser light must either pass up through the dichroic filter or reflect upward from the dichroic filter after passing through the epifluorescence light path. In either case, if the laser propagates as a plane wave through the cube (and the infinity space), it will be focused in the specimen plan. It should be noted that laser tweezers typically use wavelengths beyond the design spectrum of the microscope objective and will focus deeper than the specimen plan. This is typically advantageous as discussed below. Microscope manufactures currently design special objective lenses with long enough chromatic correction to cover the laser wavelength. If the filter cube housing the dichroic filter also houses an emitter and an exciter then they must be custom designed to pass the laser where appropriate. Similarly, the dichroic must be custom designed to pass/reflect both the visible and laser wavelengths.

3. The RoboLase Systems

RoboLase I is diagrammed in Fig. 5. It is built on an older model of Zeiss microscope (Zeiss Axiovert 100) with either a 40× (phase III, NA 1.3) or a 63× (phase III, NA1.4) oil immersion objective. RoboLase I makes special use of two Zeiss dual video adapters. The dual video adapters come standard with a 50/50 beam splitter mounted in a removable filter cube designed to hold a rectangular beam splitter (or filter) and two round filters. The filters and beams splitters can be replaced with custom-designed filters. RoboLase I uses an Nd:YVO_4 continuous wave 1064-nm wavelength laser (Spectra Physics, Model BL-106C, Mountain View, CA) for laser tweezers. The lower dual video adapter (dual video adapter I) houses a filter cube (filter cube I) containing only a long-pass dichroic filter that transmits laser light entering the left-hand port of the dual video adapter and reflects visible light coming back from the objective into the upper dual video adapter (dual video adapter II). In Fig. 5, the incoming laser light (dashed line) is shown entering the dual video adapter, while fluorescence and/or red-filtered white

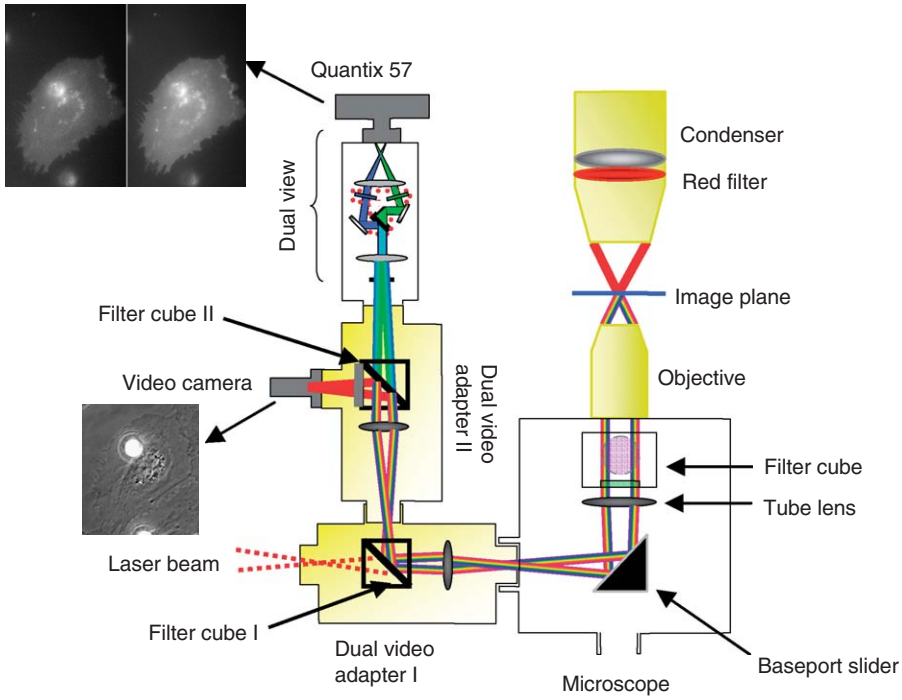

Fig. 5 Diagram of RoboLase I microscope components. An inverted microscope and two dual video adapters create a laser-scissors/FRET-imaging system. Laser light (dashed line) enters dual video adapter I and light collected by the objective lens is reflected by filter cube I toward dual video adapter II and the dual view system. A red filter is placed before the microscope condenser to separate phase-contrast imaging from shorter wavelength fluorescence emissions. Filter cube II reflects phase-contrast light toward the video camera to continuously display phase images of the microsphere and the cell (sample image shown). CFP and YFP light passes into the dual view system which splits the emissions and images two copies of the cell (CFP and YFP) simultaneously on the Quantix 57 CCD camera (sample image shown).

light (thick rainbow lines) are shown coming from the microscope objective and reflecting upward from filter cube I. In order to separate CFP and YFP fluorescence from wide-field nonfluorescence light (phase contrast), a red band-pass filter (HQ 675/50 M, Chroma Technology Corporation, Rockingham, VT) is placed above the microscope condenser. Visible light entering dual video adapter II is separated by a dichroic filter (short-pass, 650-nm cuton wavelength, Chroma Technology Corporation) housed in filter cube II. The filter cube also houses a second red band-pass filter (HQ 675/50 M, Chroma Technology Corporation). A phase-contrast image is focused onto the CCD camera (Sony, Model XC-75, New York City, NY) as shown in Fig. 5. The shorter wavelength CFP and YFP emissions pass through filter cube II and enter the dual view system (Optical Insights, Tucson, AZ). The dual view uses a 505-nm cuton wavelength long-pass dichroic filter (505 dcxr,

Chroma Technology Corporation) to separate the blue/green light as shown in Fig. 5. Each light path is further filtered by CFP/YFP emission band-pass filters centered at 470 nm (HQ 470/30, Chroma Technology Corporation) and 535 nm (HQ 535/30, Chroma Technology Corporation), respectively. When designing the band-pass filters, take care that they also block the laser wavelength to remove any scattered or reflected laser light in the system. The CFP and YFP representations of the cell are imaged side by side on a single CCD chip (Quantix 57, Photometrics, Tucson, AZ). During experiments, phase-contrast images are used to position the bead with respect to the laser focus by moving the microscope stage. Repeatability is 1 μm at best and limits the accuracy at which force can be controlled.

RoboLase I allows CFP/YFP imaging and laser trapping using standard over the counter equipment and no modifications of the microscope stand. However, it suffers from poor laser light efficiency. Laser light passes through the dual video adapter's lens system, the microscope tube lens, and the microscope objective; none of which are optimized for 1064-nm light. There is only 30% efficiency from outside the microscope to the back of the objective and 30% efficiency through the objective. Taken together, the system efficiency is at best 10%. The optics within our microscope are not antireflection coated for 1064-nm light and significant back reflection from internal lenses of the microscope and the dual video adapter leads to poor net transmission through the system.

External optics of RoboLase I are shown in Fig. 6. Two dielectric mirrors tuned to 1064 nm reflect and orient the beam parallel to the optical table and along the

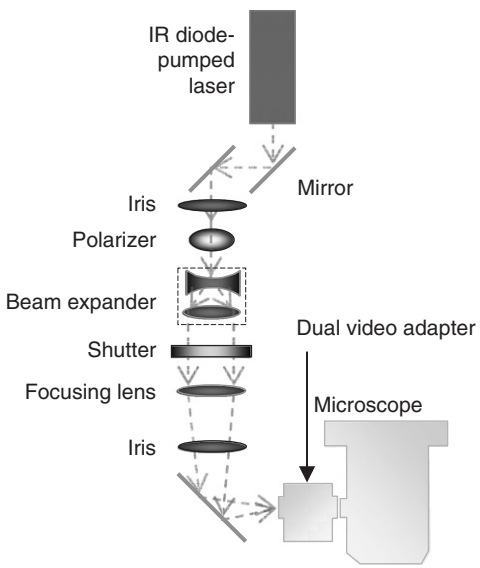

Fig. 6 External laser optics of the RoboLase I system.

optical axis of the microscope. Two antireflection-coated lenses expand the beam (plano-concave lens, $f = -25.5$ mm at $\lambda = 1064$ nm and plano-convex lens, $f = 76.2$ mm at $\lambda = 1064$ nm) in order to fill the back aperture of the microscope objective. A third antireflection-coated lens (biconvex lens, $f = 200$ mm) focuses the beam just beyond the intermediate image plane outside dual video adapter I. This lens can be moved axially in order to shift the focal position of the laser deeper into the cell culture chamber without moving the microscope objective. In this way, the axial-trapping position of a bead can be changed without changing the focal plane of the image. The focal displacement is also necessary to trap a microsphere. If the laser focus is too near the cover glass (i.e., less than the bead radius away), the trap will compress the microsphere as it attempts to pull it down through the glass and the microsphere will be ejected.

The RoboLase II system increases laser transmission efficiency by directing the laser along the epifluorescence excitation light path from the back of the microscope, as shown in Fig. 7 and previously published by Botvinick and Berns (2005). The trapping laser light source is an Ytterbium continuous wave fiber laser with a 5-mm collimator providing randomly polarized TEM00 mode 1064-nm laser output with 10-W maximum power (IPG Photonics Corporation, Oxford, MA). The epi-illumination optics were removed from a Zeiss Axiovert 200M motorized

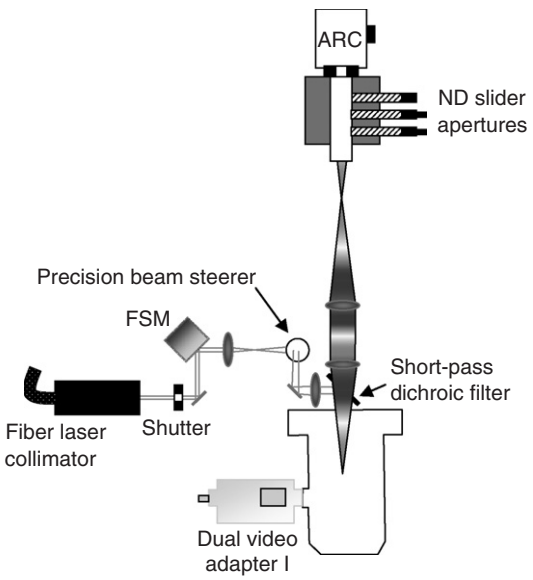

Fig. 7 External optics of the RoboLase II system. The epifluorescence light train was removed and recoupled into the microscope via two achromatic doublets. A dichroic filter combines fluorescence excitation light with laser light behind the microscope stand. The back focal plane of the objective is mapped to the surface of a fast-scanning mirror (FSM) for x, y beam steering via two antireflection-coated lenses.

microscope. The arc lamp and epioptics were positioned distal to the microscope and recoupled via two 400-mm positive achromatic doublets (Newport Corporation, Irvine, CA) antireflection coated for the visible spectrum. A short-pass dichroic mirror with a 900-nm cuton wavelength was placed just behind the microscope stand to reflect laser light into the microscope while passing light from the arc lamp. In this setup, the laser neither passes through a tube lens, the epifluorescence lens system, or any lens not antireflection coated for the laser wavelength. The laser trap is steered within the specimen plane by a motorized two-axis mirror mount placed conjugate to the back focal plane of the objective (FSM-300-01 Fast Scanning Mirror, ER.1 coating, Newport Corporation). The fast scanning mirror has a 3-μrad repeatability along both axis, corresponding to a 0.001-V change at its controller's analog input. Analog signals are created by a 12-bit data acquisition board (PXI 6711, National Instruments, Austin, TX) with 0.005-V resolution in the range -10 to 10 V. With a 63$\times$ (phase III, NA 1.4) objective and the scan and tube lenses, a 3-μrad mirror deflection corresponds to 2.6-nm displacement in the specimen plane. Therefore, RoboLase II has a 13-nm pointing resolution. The laser transmission efficiency is 75% from the laser collimator to the back aperture of the objective and 30% through the objective.

RoboLase II employs a similar strategy to separate phase contrast from CYF/YFP emission as found in the dual video adapter II of RoboLase I. The fluorescent filter cube housed in the reflector turret of the microscope stand is custom designed to pass both arc lamp and laser light through the exciter and to reflect them from the dichroic filter. CFP/YFP emissions are then separated with a dual view-imaging device with identical optics to that of RoboLase I. During experiments, the laser is steered near to the edge of the bead and can be steered throughout the experiment without moving the microscope stage.

In RoboLase III, we mix laser tweezers with multiphoton excitation. In this system, a custom-built filter cube is mounted in the reflector turret so that it is rotated 90° counterclockwise (top view) about the optical axis of the objective lens. The reflection turret is modified so that light enters the left-hand side of the microscope (top view) and is reflected upward into the microscope objective. With the cube in place, light from the epiflorescence port would hit the edge of the mirror and not be reflected in to the objective lens. Instead, RoboLase III uses a TrimScope (TauTech, Columbia, MD) which multiplexes the femtosecond-pulsed laser (MaiTai Broadband, 710- to 990-nm tuning, 100-fs pulse width; Newport Corporation) into multiple beams forming a linear array of diffraction-limited spots in the specimen plane. The TrimScope scans the array to produce multiphoton images. The TrimScope is equipped with a short-pass dichroic filter mounted in the custom filter cube to reflect laser light up into the objective, while passing returning fluorescence emission down toward the camera port. We mounted a short-pass dichroic with cuton wavelength 1000 nm (DCPS 1000, Chroma Technology Corporation) in between the tube lens and scan lens of the TrimScope in order to mix 1064-nm trapping laser with the broad range of femtosecond wavelengths. The efficiency of this system is 50% from the laser head to the back aperture of the

objective and about 30% through the objective. But efficiency from outside the microscope to the back aperture is 85% and is limited by the dichroic in the filter cube.

4. Calibrating the Laser Tweezers

In mechanobiology experiments, it is often necessary to maximize force generation on beads adhered to a cell. Large forces are generated by steering the trap focus near to the edge of the microsphere, which is held more-or-less in place by its connections to the cell. According to Ashkin (1992), the maximum transverse force is generated by focusing the laser trap just shy of the microsphere's surface (98% of the radius) in a transverse plane through the center of the microsphere. Near the surface of the microsphere the bead to beam displacement is not linearly related to restoring force and implementation of a quad detector with a linear spring model is not appropriate. However, a quad detector can be used to measure bead to beam displacement with a nonlinear calibration. Microspheres can be visualized by the CCD camera in the red light path (Fig. 5) of the RoboLase systems. Using the Airy disk radius as an approximation of microscope resolution, the spatial sampling frequency and thus accuracy of positioning of the bead image on the CCD can be calculated. With the addition of a secondary zoom lens (not shown), the bead can be sufficiently over sampled to determine the bead position with accuracy greater than the Airy disk radius. Sheetz *et al.* have reported measuring the position of micron-size beads with 5- to 10-nm resolution (Felsenfeld *et al.*, 1999; Gelles *et al.*, 1988).

The force calibration is best performed on a microsphere trapped above a cover glass with no cells in culture. Moving the stage along a square wave trajectory with sufficient amplitude allows the bead to reach force equilibrium before it changes directions. The force equilibrium is reached when viscous forces equate to light forces. The bead to beam displacement should be measured for a range of laser powers or stage velocities so that the observed displacements range from zero to near the bead radius. Since the relationship between the optical force and the laser power is linear, the calibration can be done at a lower laser power and thus lower stage speeds, and then scaled later to higher laser powers. It is not recommended to rely on a mathematical fit to extrapolate the force–displacement relationship. Care should be taken to measure the relationship for the full range of displacements about the operating point (i.e., the microsphere edge). Viscous force can be calculated from stage velocities using the stokes flow approximation

$$F_{\text{viscous}} = 6\pi\eta r v_{\text{stage}}$$

where η is the viscosity of the surrounding fluid (e.g., water at room temperature), r is the microsphere radius, and v_{stage} is the microscope stage velocity. It is not recommended to steer the beam during calibration. The calibration can be repeated for different beam locations in the field of view to determine the spatial distribution

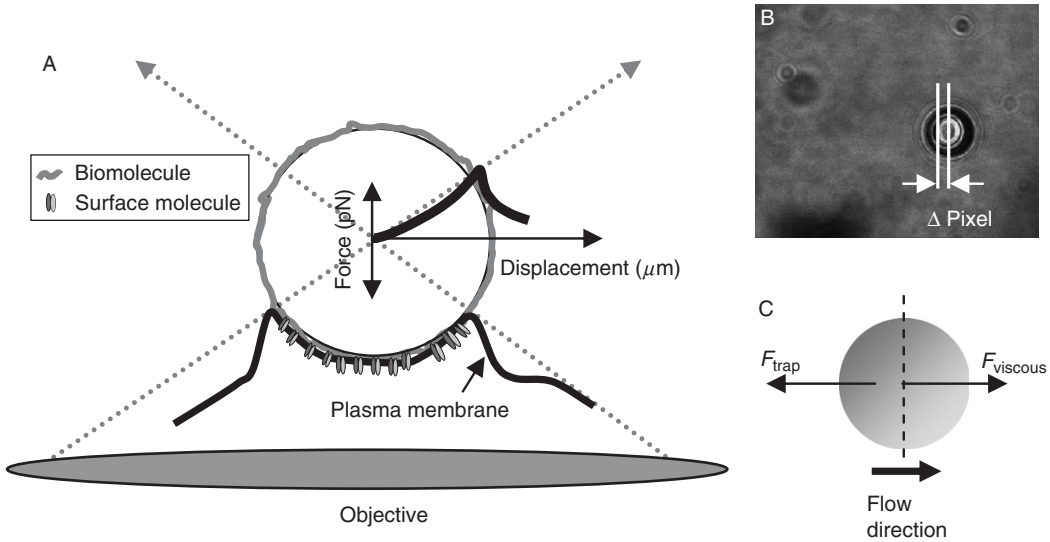

Fig. 8 Diagram of laser-tweezers calibration. (A) During experiments, a microsphere coated with a specific biomolecule is rigidly attached to the cell through the cell's complementary surface molecules. The trapping laser is focused into the microsphere to produce forces. As shown, the focus is aligned with the microsphere center and no force is exerted (ignoring scatter forces). As the focus is steered toward the bead surface, the laser light exerts increasing force on the microsphere as demonstrated by the superimposed graph where "displacement" is the center to focus distance and the "force" acts transversely to pull the center toward the focus. (B) a microsphere freely suspended in water is trapped as the stage moves at constant velocity to the right. The two vertical white lines indicate the bead's center and the focus' horizontal coordinate. The displacement Δx is indicated. (C) Illustration of microsphere in a rightward flow field with viscous and laser trap forces in balance. When the microsphere is in force equilibrium, the viscous force is equal in magnitude to the laser trap force. A calibration is performed by recorded Δx for a set of stage velocities and thus laser forces. During bead adhesion experiments, as Δx is known, the force can be determined.

of trap strength. The trap strength can change throughout the field if the beam is not telescopically steered, and in general will change due to imperfections in system optics. Figure 8 demonstrates the calibration process.

5. Image Processing

Once images have been acquired they must be processed in a manner appropriate to what is being quantified. For example, if the experiment seeks a binary answer as would be the case for a live/dead assay with propidium iodide, image processing is straight forward and most canned algorithms would be appropriate. If the experiment seeks to map out fluorescence intensity, or to determine fine structures within the cell, or near the edge of the cell itself, care must be taken in assigning a value to

each pixel. For the case of imaging the Src reporter with one of our RoboLase systems, the following procedures are applied: extraction of the CFP and YFP subimages from the raw image, pixel registration between the two subimages, extraction of the cell from the background, subtraction of background signal, and calculation of the ratio image.

As shown in Fig. 5, the dual view system images both the CFP subimage and the YFP subimage onto the CCD simultaneously. The extraction of the two subimages can be as trivial as dividing the raw image in two, if care is taken while aligning the dual view system. Alternatively, two regions of interest of identical dimension can be extracted around the two subimages. RoboLase II uses an Orca AG (C4742–80–12AG, Hamamatsu, Bridgewater, NJ) CCD camera with 1344 $\times$ 1024 pixels (6.45 μm^2). The CFP subimage is extracted as the first 1344/2 columns and the YFP subimage begins at the 1344/2 + 1 column and ends at the end of the raw image.

The next step is to test the pixel registration between the two subimages. That is, to make sure each pixel CFP(x_i, y_j) corresponds to pixel YFP(x_i, y_j) for all i, j where x and y are the Cartesian coordinates of each pixel within the subimage. We use the corr.m function in Matlab (The Mathworks, Inc., Natick, MA) to compute the Pearson's linear correlation coefficient between the two images. The correlation is called recursively as the YFP subimage is cropped by a sliding region of interest that includes all but a boarder region about the subimage. The CFP subimage is cropped only once so that each calculated correlation represents a relative shift between the two subimages. We then choose the shift which best correlates the two subimages. The two cropped images, shift included, now constitute the new subimages, which are further analyzed as described below.

Now that the two CFP and YFP subimages have been coregistered, image segmentation must be applied to extract the pixels belonging to the cell from pixels belonging to the background. In this way, we can specify for which pixels the ratio should be calculated, and we can determine the proper background value to be subtracted before the ratio is calculated. It is critical to remove the background bias in order to compare ratio values between different cells. The ratio should only be calculated for pixels in which both the CFP and YFP values are above the noise floor. With the dual view system, neutral density filters can be used on the YFP channel in order to balance the relative brightness between the CFP and YFP channels. We do not implement this strategy in our laboratory as the YFP channel does not typically fill up its electron well capacity within the time of image integration ($\sim$1 s). Since the CFP channel is dimmer, it is segmented and the resulting binary mask is applied to both the CFP and the YFP subimages. If image segmentation were calculated from the YFP subimage, pixels in the YFP subimage would be selected for which the corresponding CFP pixels would be in the noise floor. Ratios calculated for these pixels would be inversely correlated to the YFP brightness (where ratio is CFP/YFP) and would not represent a physiological measurement.

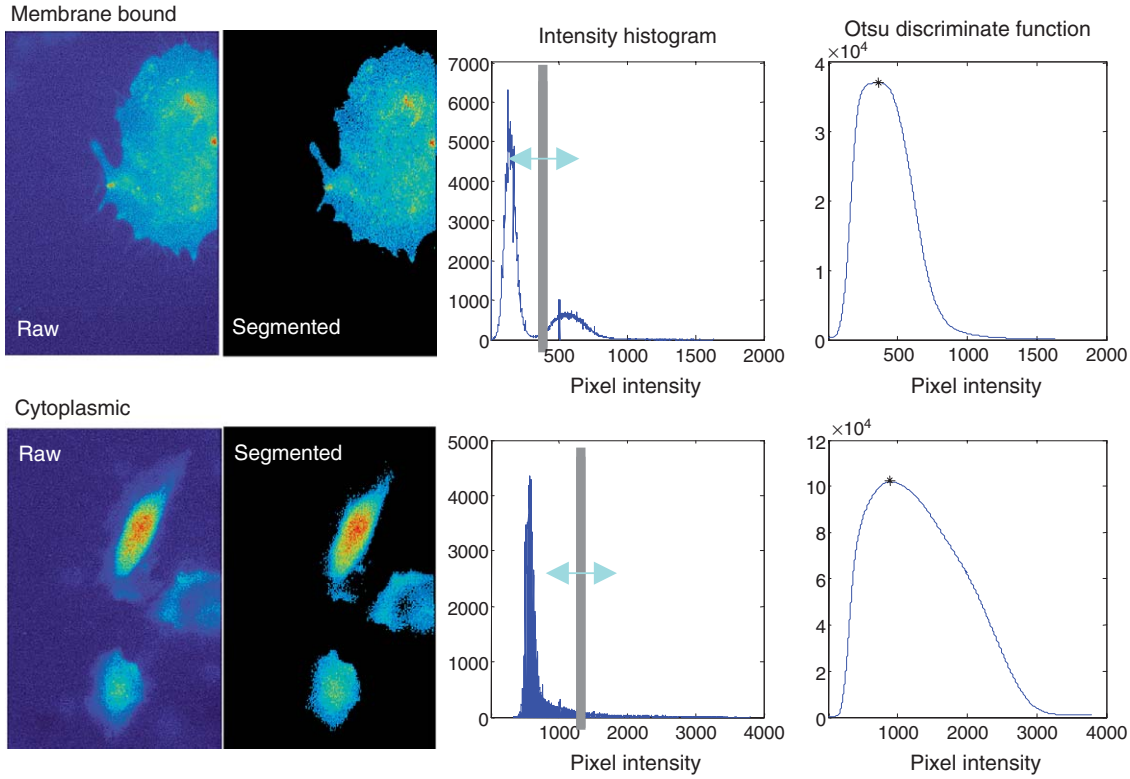

Fig. 9 Two-class thresholding fails on images of cytoplasmically distributed biosensor. (Top row) HUVEC cell labeled with membrane-bound biosensor. A raw image is shown in pseudo-color followed by its segmented image. The image was segmented using the two-class Otsu's method and shown in the next image. The background pixels (black) have been suppressed. The intensity histogram is bimodal and the two-class Otsu's method's discriminate function takes on a maximum value in between the two modes. (Bottom row) Huevec cell labeled with cytoplasmically distributed biosensor. The pseudo-color raw image shows narrow differences between background and cell edge values. The segmented image incorrectly mapped dim pixels at the cell edge and podia to the background. The intensity histogram is not bimodal and choosing the maximum value of the discriminate function does not separate the cell from the background.

Figure 9 represents two typical cases of image segmentation. The top row contains a raw CFP image, shown in pseudo-color, of a plasma membrane-bound fluorescent biosensor. Fluorescent intensity within the cell is somewhat uniform and application of a two-class Otsu's method threshold correctly removes the cell (shown in pseudo-color) from the background (black). As can be seen by the image's intensity histogram, pixel values have a bimodal distribution. The ubiquitous two-class Otsu's method evaluates a discriminate function for each potential threshold value, as indicated by the sliding gray column in the histogram. Otsu's

method chooses the threshold value corresponding to the maximum value of the Otsu's method discriminate function. For the membrane-bound biosensor, the maximum value corresponds to a threshold value which sufficiently separated the background from the cell. The bottom row of the figure shows a raw CFP image of a similar biosensor that is not membrane bound, but distributed within the cytoplasm. This cell is brightest in the nuclear region and very close to background values in the thin podia regions. Application of a two-class Otsu's method mistakenly maps the thinnest region of the podia to the background, and any further analysis on the image would not include those pixels. In the study of mechanobiology, the pixels in the podia are often crucial to the experiment. As can be seen, the intensity distribution is not bimodal so it is not surprising that a two-class system cannot segment the cell well. The maximum value of the discriminate function cannot separate the podia from the background.

Instead, we implement a custom-designed iterative three-class method based on the generalized Otsu's method. Figure 10 demonstrates the method. For each

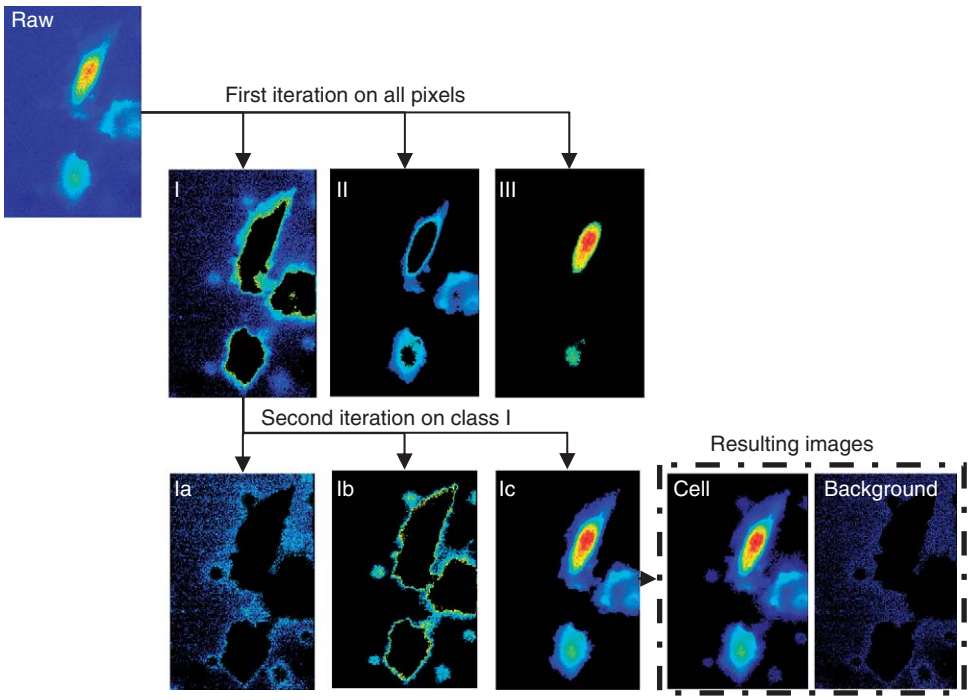

Fig. 10 Segmenting the cytoplasmically distributed biosensor image using an iterative three-class Otsu's method. In the first iteration, three classes are created, the dimmest (class I) containing both background and dim cell pixels. The second iteration acts on class I pixels and creates three new classes, Ia, containing background pixels; Ib, containing dim cell pixels; and Ic, containing the remaining cell's pixels. Two images result representing background and cell (union of Ib and Ic) pixels.

iteration, the input pixels are separated into three pixel classes. The following Matlab code operates on "input_image", which contains all pixels to be analyzed, and returns two threshold values which create three pixel classes. The code was adapted from Matlab's two-class method and from Liao *et al.* (2001). The algorithm seeks threshold 1 (k_1) and threshold 2 (k_2) within the intensity range $1 < k_1 < k_2 < L$ to create three pixel classes c_1, c_2, and c_3 such that:

$$c_1[1 \ldots k_1];\ c_2[k_1 + \mathrm{i} \ldots k_2];\ c_3[k_2 + 1 \ldots L]$$

$$\omega_i = \sum_{c_i} P_i \ldots \mu_i = \sum_{c_i} \frac{iP_i}{\omega_i}$$

$$\sigma_b^2 = \omega_1\mu_1^2 + \omega_2\mu_2^2 + \omega_3\mu_3^2$$

where σ_b^2 should be maximized at k_1 and k_2.

```
input_image = double(input_image); % Convert to double precision
max_bin = (max(input_image(:))); % Calculate the max and min values
min_bin = (min(input_image(:)));
[counts,thresholds] = hist(input_image(:),max_bin-min_bin + 1);
L = length(thresholds); % size of intensity value range
P = (zeros(L)); S = (zeros(L)); %initialize P and S

% Calculate first row of P and S
f = counts/sum(counts); % normalize frequencies
P(1,:) = cumsum(f);
S(1,:) = cumsum(f.* (min_bin:max_bin));

%Calculate the rest of P and S
for n = 2:L
  P(n,n:L) = P(1,n:L) - P(1,n - 1);
  S(n,n:L) = S(1,n:L) - S(1,n - 1);

end

% Calculate H
H = S.^2./P;

% calculate initial guess for first threshold
temp = [];
for t1 = 1:L - 2%first threshold
  temp(t1) = H(1,t1) + max(H(t1 + 1,t1 + 1:L));
end
thresh1 = round(mean(find(temp == max(temp))));

% calculate initial guess for second threshold
temp = [];
for t2 = thresh1 + 1:L - 1%second threshold
```

```
    temp(t2) = H(thresh1 + 1,t2) + max(H(t2 + 1,t2 + 1:L));
end
thresh2 = round(mean(find(temp == max(temp))));
% calculate discriminate function between the two initial guesses
for t1 = 1:thresh1
    for t2 = thresh1 + 1:thresh2
        sigma_b_squared(t1,t2) = H(1,t1) + H(t1 + 1,t2) + H(t2 + 1,L);
    end
end

% find max discriminate function value and corresponding thresholds
index = max(max(sigma_b_squared));
[thresh1,thresh2] = find(sigma_b_squared == index);
thresh1 = uint16(mean(thresh1));
thresh2 = uint16(mean(thresh2));

% thresholds reference num_bins and not the absolute pixel value.
% Divide max(I(:)) by num_bins and map thresholds to indices of that array.

thresh1 = round(thresholds(thresh1)); %thresh1 is index pointing to thresholds
    bin centers
thresh2 = round(thresholds(thresh2)); %thresh2 is index pointing to thresholds
    bin centers
```

In Fig. 10, the first iteration of image segmentation operates on the raw image of a cell with a CFP probe distributed in the cytoplasm. The three resulting pixels classes are shown. Class III contains the brightest pixels (nuclear region), and class II contains pixels of the cytoplasmic region surrounding the nuclear region. Class I contains both the background pixels and those of the thin regions of the cell. The second iteration of image segmentation operates on class I pixels to yield three new classes Ia, Ib, and Ic. Ia contains only background pixels, Ib contains the podia and thin edges of the cell, and class Ic contains all remaining cell pixels. Two resulting images are formed, the background pixels (Ia) and the cell pixels (union of Ib and Ic). A binary mask of cell pixels can be constructed from the union of classes Ib and Ic coordinates.

Figure 11 demonstrates the process of transforming a raw CCD image into a ratio image. The raw image contains both the CFP and YFP copies of the cell and is first separated into its two subimages, labeled CFP and YFP in the figure. Pixel registration through image correlation (not shown) is applied and a binary mask (labeled mask) is created by segmenting the raw CFP subimage. CFP and YFP subimages are then masked whereby values are kept if their corresponding mask values are "1" and are set to 0 otherwise. Subimage pixel values corresponding to mask "0" values are averaged as an estimate of the image background intensity. The background estimate is then subtracted from each subimage. The ratio image is calculated by dividing the masked and background-subtracted CFP values by the masked and background-subtracted YFP values:

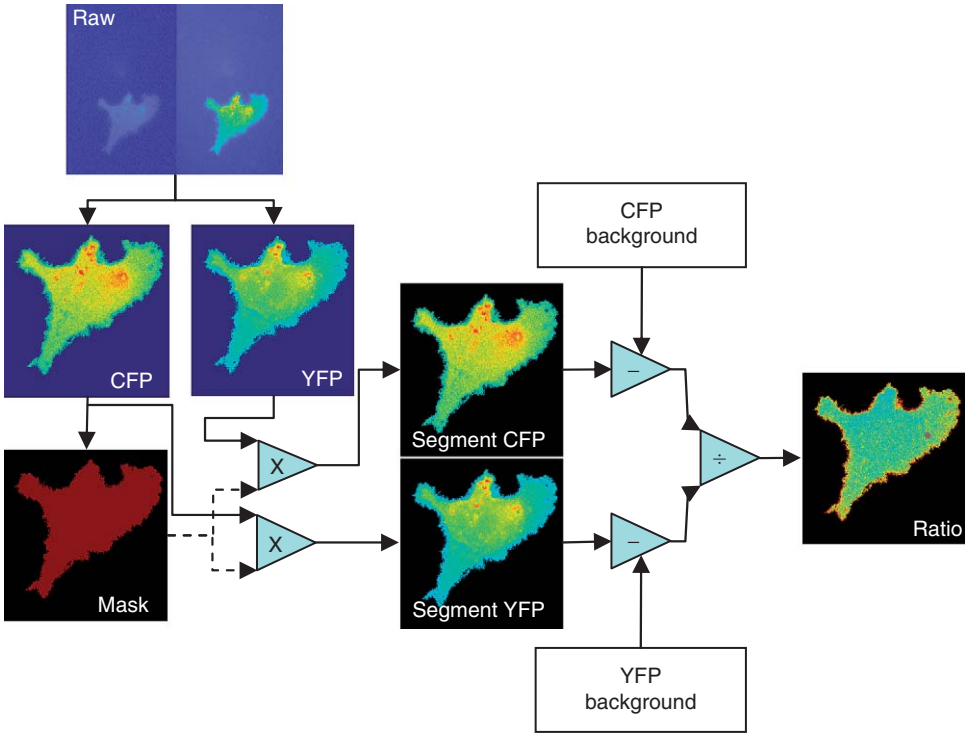

Fig. 11 Demonstration of calculating a ratio image. A raw image contains the CFP and YFP copies of the cell. Two ROIs of identical dimension (not shown) crop the CFP and YFP subimages from the raw image. Two ROIs may have a relative shift to compensate for misalignment of the system (see text). The CFP subimage is segmented to create a binary mask which is applied to both the CFP and the YFP subimages through image multiplication. The CFP- and YFP-segmented images have the mean background value subtracted from each (only subtracting from nonzero pixels) where the mean background is calculated from class Ia pixels (see Fig. 10). The resulting CFP subimage is divided by the resulting YFP image in a pixel-by-pixel manner to form the ratio image.

$$\text{Ratio}(x_{i,j}, y_{i,j}) = \frac{\text{CFP}(x_{i,j}, y_{i,j})}{\text{YFP}(x_{i.j}, y_{i,j})}$$

6. Quantifying Kinase Activity

Once the ratio image has been calculated, the distribution of ratios within one image and across time can be analyzed to extract physiological measurements from the experiment. Three methods used commonly in our laboratory are evaluation of ratio histograms, analysis of distal pixel activation, and polarity analysis. Figure 12A and B plot the distribution of ratio values for cells expressing the membrane-bound FRET Src reporter. Higher ratio values indicate increased fraction of phosphorylated biosensor within the corresponding cell voxel. Histograms are plotted for two

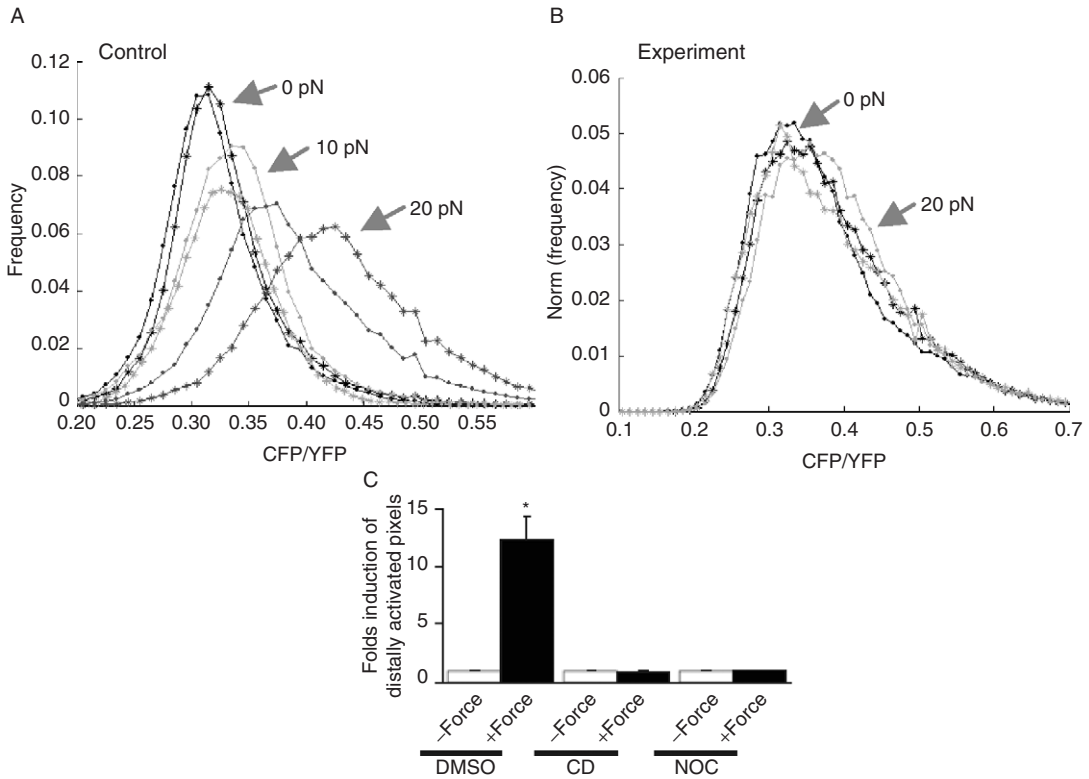

Fig. 12 Analysis of ratio-value frequency distribution and distal activation for HUVECs with membrane-bound Src reporter. (A) Frequency plots of ratio values indicate Src activation within a cell following pulling on an attached microsphere. In a control experiment, the histogram shifts rightward following pulling at 10 pN as more pixels contain a greater fraction of activated Src. Pulling at 20 pN further shifts the histogram and populates the right tail of the distribution indicating a cell-wide trend toward higher ratios and thus great Src activation. (B) Histograms for experimental cell for which long-range mechanotransduction may be compromised. No significant histogram shift occurs following pulling at 20 pN indicating to significant activation of Src throughout the cell. (C) Example of distal pixel activation analysis taken from Wang *et al.* (2005, p. 10). Pixels are counted if they are more than the half the virtual cell radius (see text) from the microsphere center, and greater in ratio value than the 80th percentile ratio from baseline measurements (i.e., before pulling). A low concentration of DMSO was applied to the cell as control and pulling led to a 12-fold increase in activated pixels indicating long-range force activation of Src. Disruption of the cytoskeleton by cytochalasin D or nocodazole suppressed the count indicating that distal locations in the cell did not have an increase in activated Src.

baseline measurements, after pulling on adhered fibronectin-coated 10-μm-diameter microspheres at the indicated force level. The control experiment (Fig. 12A) has two baseline (measurements taken after bead adhesion but before pulling) measurements taken 2 min apart, measurements taken immediately and 5 min after pulling at 10 pN, and measurements taken immediately and 3.5 min after pulling at 20 pN.

As can be seen, the baseline was consistent, while pulling at 10 pN immediately shifted the histogram to the right. This represents an increase in Src signaling throughout the cell as more pixels took on higher ratios as compared to baseline. After 5 min of 10-pN force, the histogram shifted again by a similar distance. On pulling at 20 pN, the histogram shifted to the right again. The shift occurred in both the ratio of peak frequency and in the right-hand tail which was elevated from the floor. The ratio 0.3, which was most frequent at baseline, has been quelled, while the ratio 0.43 which was infrequent at baseline has become most frequent after 3.5 min of pulling at 20 pN. This indicates a significant shift in the Src activation profile in the cell and a global increase in the activated state. Figure 12B shows an experimental cell in which transduction of the force has been compromised. The two baseline distributions taken 3.5 min apart are not different from the distribution measured immediately or 6.5 min after pulling at 20 pN. This type of analysis gives insight into whole cell activation of Src kinase, but does not elucidate the spatial distribution of activated pixels (or ratios) within the cell.

One method of addressing spatial distribution is to examine the distribution of ratios in regions of the cell distal to the attached microsphere. The first step is to define which pixels are distal to the bead. In Wang *et al.* (2005), the boundary separating distal pixels from proximal ones was defined as half the virtual radius of the cell (R)

$$\frac{R}{2} = \frac{1}{2}\sqrt{\frac{A}{\pi}}$$

where A is the area of the cell (or the pixel count of the cell mask). A pixel at coordinate (x, y) is considered distal from the bead center (x_0,y_0) if the Euclidian distance between them is greater than $R/2$ as calculated by:

$$\sqrt{(x-x_0)^2+(y-y_0)^2} > \frac{R}{2} = \frac{1}{2}\sqrt{\frac{A}{\pi}}.$$

The next step is to determine what ratio value within a baseline image of a cell is greater than a percentile of all pixels in that cell (e.g., 80%, 85%, 90%, and so on) at baseline. In subsequent images, the number of pixels that have ratios above that value and are distal to the bead are counted. The fold increase between baseline and pulling can be calculated as a means of measuring the degree to which distal pixels were activated by mechanical transduction through the cell. In Fig. 12C, an 80% threshold was used (Wang *et al.*, 2005). In this figure the control (DMSO) group had a 12-fold induction postpulling, while the two experimental groups (CD, cytochalasin D and NOC, nocodazole) had no significant increase in activated pixels. This method indicates that interruption of the cytoskeleton precludes long-range Src activation as compared to the control.

The spatial distribution can be further examined by measuring Src activation as a function of angular deviation from the direction of pulling. We call it polarity analysis. In Matlab, this operation is easily computed by transforming the original

Cartesian pixel coordinates into polar coordinates. The coordinates of the bead's center must first be subtracted from the coordinates of each pixel, thus moving the origin to the bead center. The (x,y) coordinates can be transformed into polar coordinates (r, θ) by the equations:

$$r = \sqrt{(x - x_0) + (y - y_0)}$$

$$\theta = \tan^{-1}\left(\frac{y}{x}\right)$$

where the four quadrant arctan function "atan2" is called. Positive θ is in the counterclockwise direction, and θ values are adjusted so that 0° corresponds to the direction of pulling. Coordinates are then sorted by increasing θ and the data can be divided into bins, or slices, defined by equally spaced intervals of θ. The distribution of ratio values within each slice can then be analyzed. In Fig. 13, two cells expressing the membrane-bound Src reporter have been analyzed. The top row shows cell 1's ratio images at baseline ($T = 0$ min), after 16.5 min of pulling the bead downward at 10 pN and after 12 more minutes pulling downward at 20 pN. The base of the red arrow and the crosshair indicates the bead center. The cell was divided into 36 slices and the mean and standard deviation of each slice is graphed as a function of angle. Notice that maximum activation occurs at angles 110°–180° which are opposite to the direction of pulling. Cell 2 was subjected to an experimental protocol which may adversely affect long-range mechanotransduction. As can be seen by the ratio images in the bottom row of Fig. 13, the extent of long-range signaling is diminished as compared to cell 1, with little changes away from cell edges. Cell 2 was pulled at twice the force as cell 1, or 20 and 40 pN. The graph of mean and standard deviation of activation as a function of angle shows a slight increase in ratio opposite to the direction of pull after 6.5 min of pulling at 20 pN. After 12 additional minutes pulling at 40 pN, activation is elevated throughout the cell with a maximum still opposite pulling. The maximum activation level of cell 2 after pulling at 40 pN is nearly equal to the minimum activation level of cell 1 after pulling at 20 pN. It should be noted that for both cells the response to each force level was nearly instantaneous, and did not appreciably increase as the force was held at a constant level.

IV. Summary and Future Direction

The integration of genetically encoded FRET biosensors and laser tweezers has been proved to be vital for studying mechanotransduction in live cells with high spatiotemporal resolution. Further development of new FRET-based biosensors and novel implementations of laser tweezers are expected to be the forefront research in this field in the near future. FRET technology can be applied for the biosensor designation of not only tyrosine kinases, but also serine/threonine kinases, proteases, small GTPases, and other signaling molecules. In fact, a FRET-based biosensor

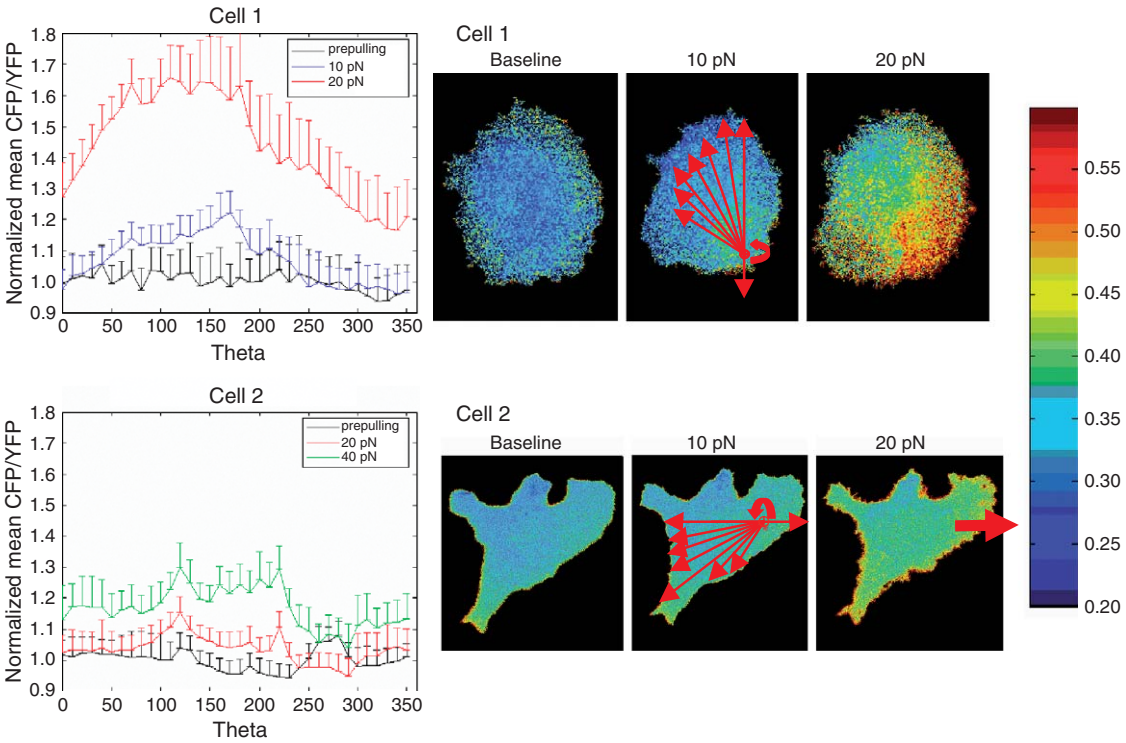

Fig. 13 Polarity analysis of Src activation. Translation of the Cartesian origin to the microsphere center and projection into polar coordinates creates a coordinate system composed of radial distance from the microsphere and angular deviation from the direction of pulling. The cells are sliced into angular bins and mean changes of Src activity can be monitored. (Top row) Cell 1 is a control cell for which an FN-coated bead is attached and pulled downward. Ratio images are shown for baseline and after pulling at 10 and 20 pN. Each cell is divided into slices indicated by red arrows centered about the bead. Graphs of mean and standard deviation as a function of angle demonstrate the polarity in Src activation within the cell. As can be seen, pulling at 10 pN increases activation about 160°, which is opposite the direction of pulling. Pulling at 20 pN substantially increases signaling throughout the cell with peak activation opposite the force. (Bottom row) Cell 2 is a control cell with compromised mechanotransduction. Pulling at 20 pN marginally increases activation, with slightly elevated signal from 110° to 180°. Pulling at 40 pN uniformly shifts the curve vertically with a peak activation value about equal to the minimum activation value observed when pulling cell 1 at half the force. This suggests a compromise in cell 2's long-range and directional sensitivity to force.

for nonenzymatic membrane receptor molecule integrin has been successfully developed (Kim *et al.*, 2003). The directed evolutionary strategies together with fluorescence-activated cell sorting (FACS) should provide a high-throughput means to develop novel biosensors. Because the excitation and emission wavelengths of CFP and YFP are relatively short and not suitable for *in vivo* imaging, it will be very desirable to develop FP pairs for FRET with longer wavelengths, ideally in the range of dark red or infrared.

The field of optical manipulation is likewise moving in a direction which will open up our understanding of cellular mechanotransduction. In addition to pulling on particles attached to the cell by specific ligand interactions, laser tweezers can be used to apply fluid sheer stress by optically rotating tapped particles (Bishop *et al.*, 2004). In this way, mechanical stresses and shear can be carefully applied to a subregion of the cell through fluid flow. Additionally, the rotating particles can be analyzed to measure the apparent viscosity of the surrounding media. As multiplexing of the trapped beam and advancements in rotating particles (Grier, 2003), both within and outside of cells, become mainstream technologies, the mechanisms of mechanotransduction will unfold from the molecular level up to the function of intact tissues in the normal and disease states.

Acknowledgments

We would like to thank Professor Shu Chien and the Whitikar Institute of Biomedical Engineering for the support, advice, and cooperation on this project. Thanks to Professor Michael Berns for his encouragement, advice, and supervision over the laser tweezers and imaging system, and for the idea that a laser can and should be brought through a microscope. E.B. would like to thank the Beckman Foundation and its Beckman Fellows award for launching his career and allowing him to build the laser tweezers and FRET system. Y.W. would like to thank the Department of Bioengineering and Beckman Institute for Advanced Science and Technology at University of Illinois, Urbana-Champaign, Wallace H. Coulter Foundation for their support.

This project was funded through the Beckman Foundation and through a grant from the US Air Force (AFOSR No. F9620-00-1-0371).

References

Ashkin, A. (1992). Forces of a single-beam gradient laser trap on a dielectric sphere in the ray optics regime. *Biophys. J.* **61**(2), 569–582.

Beningo, K. A., Dembo, M., Kaverina, I., Small, J. V., and Wang, Y. L. (2001). Nascent focal adhesions are responsible for the generation of strong propulsive forces in migrating fibroblasts. *J. Cell Biol.* **153**(4), 881–888.

Bishop, A., Nieminen, T., Heckenberg, N., and Rubinsztein-Dunlop, H. (2004). Optical microrheology using rotating laser-trapped particles. *Phys. Rev. Lett.* **92**(19), 1981041–1981044.

Botvinick, E. L., and Berns, M. W. (2005). Internet-based robotic laser scissors and tweezers microscopy. *Microsc. Res. Tech.* **68**(2), 65–74.

Chen, K. D., Li, Y. S., Kim, M., Li, S., Yuan, S., Chien, S., and Shyy, J. Y. (1999). Mechanotransduction in response to shear stress: Roles of receptor tyrosine kinases, integrins, and Shc. *J. Biol. Chem.* **274**(26), 18393–18400.

Chien, S., Li, S., Shiu, Y. T., and Li, Y. S. (2005). Molecular basis of mechanical modulation of endothelial cell migration. *Front. Biosci.* **10,** 1985–2000.

Felsenfeld, D. P., Schwartzberg, P. L., Venegas, A., Tse, R., and Sheetz, M. P. (1999). Selective regulation of integrin–cytoskeleton interactions by the tyrosine kinase Src. *Nat. Cell Biol.* **1**(4), 200–206.

Gelles, J., Schnapp, B. J., and Sheetz, M. P. (1988). Tracking kinesin-driven movements with nanometre-scale precision. *Nature* **331**(6155), 450–453.

Grier, D. G. (2003). A revolution in optical manipulation. *Nature* **424**(6950), 810–816.

Hu, S., Eberhard, L., Chen, J., Love, J. C., Butler, J. P., Fredberg, J. J., Whitesides, G. M., and Wang, N. (2004). Mechanical anisotropy of adherent cells probed by a three-dimensional magnetic twisting device. *Am. J. Physiol. Cell Physiol.* **287**(5), C1184–C1191.

Ingber, D. E. (2003a). Tensegrity I. Cell structure and hierarchical systems biology. *J. Cell Sci.* **116**(Pt. 7), 1157–1173.

Ingber, D. E. (2003b). Tensegrity II. How structural networks influence cellular information processing networks. *J. Cell Sci.* **116**(Pt. 8), 1397–1408.

Kaufman, D. A., Albelda, S. M., Sun, J., and Davies, P. F. (2004). Role of lateral cell–cell border location and extracellular/transmembrane domains in PECAM/CD31 mechanosensation. *Biochem. Biophys. Res. Commun.* **320**(4), 1076–1081.

Kernan, M., and Zuker, C. (1995). Genetic approaches to mechanosensory transduction. *Curr. Opin. Neurobiol.* **5**(4), 443–448.

Kim, M., Carman, C. V., and Springer, T. A. (2003). Bidirectional transmembrane signaling by cytoplasmic domain separation in integrins. *Science* **301**(5640), 1720–1725.

Liao, P.-S., Chen, T.-S., and Chung, P.-C. (2001). A fast algorithm for multilevel thresholding. *J. Comput. Inf. Sci. Eng.* **17**(5), 713–727.

Miyawaki, A., Llopis, J., Heim, R., McCaffery, J. M., Adams, J. A., Ikura, M., and Tsien, R. Y. (1997). Fluorescent indicators for Ca^{2+} based on green fluorescent proteins and calmodulin. *Nature* **388**(6645), 882–887.

Pelham, R. J., Jr., and Wang, Y. (1997). Cell locomotion and focal adhesions are regulated by substrate flexibility. *Proc. Natl. Acad. Sci. USA* **94**(25), 13661–13665.

Riveline, D., Zamir, E., Balaban, N. Q., Schwarz, U. S., Ishizaki, T., Narumiya, S., Kam, Z., Geiger, B., and Bershadsky, A. D. (2001). Focal contacts as mechanosensors: Externally applied local mechanical force induces growth of focal contacts by an mDia1-dependent and ROCK-independent mechanism. *J. Cell Biol.* **153**(6), 1175–1186.

Thomas, S. M., and Brugge, J. S. (1997). Cellular functions regulated by Src family kinases. *Annu. Rev. Cell Dev. Biol.* **13,** 513–609.

Ting, A. Y., Kain, K. H., Klemke, R. L., and Tsien, R. Y. (2001). Genetically encoded fluorescent reporters of protein tyrosine kinase activities in living cells. *Proc. Natl. Acad. Sci. USA* **98**(26), 15003–15008.

Tsien, R. Y. (1998). The green fluorescent protein. *Annu. Rev. Biochem.* **67,** 509–544.

Wang, N., Butler, J. P., and Ingber, D. E. (1993). Mechanotransduction across the cell surface and through the cytoskeleton. *Science* **260**(5111), 1124–1127.

Wang, Y., Botvinick, E. L., Zhao, Y., Berns, M. W., Usami, S., Tsien, R. Y., and Chien, S. (2005). Visualizing the mechanical activation of Src. *Nature* **434**(7036), 1040–1045.

Wang, Y., Miao, H., Li, S., Chen, K. D., Li, Y. S., Yuan, S., Shyy, J. Y., and Chien, S. (2002). Interplay between integrins and FLK-1 in shear stress-induced signaling. *Am. J. Physiol. Cell Physiol.* **283**(5), C1540–C1547.

Zhang, J., Ma, Y., Taylor, S. S., and Tsien, R. Y. (2001). Genetically encoded reporters of protein kinase A activity reveal impact of substrate tethering. *Proc. Natl. Acad. Sci. USA* **98**(26), 14997–15002.